Title

A three-dimensional modular adaptable grid numerical model for light propagation during laser irradiation of skin tissue

Journal

IEEE Journal on Selected Topics in Quantum Electronics, 2(4)

ISSN

1077-260X

Authors

Pfefer, TJ
Barton, JK
Chan, EK
et al.

Publication Date

1996-12-01

DOI

10.1109/2944.577318

A Three-Dimensional Modular Adaptable Grid Numerical Model for Light Propagation During Laser Irradiation of Skin Tissue

T. Joshua Pfefer, Jennifer Kehlet Barton, Eric K. Chan, Mathieu G. Ducros, Brian S. Sorg, Thomas E. Milner, J. Stuart Nelson, and Ashley J. Welch, *Fellow, IEEE*

***Abstract*— Information regarding energy deposition during laser irradiation of structurally complex biological tissue is needed to understand and improve the results of clinical procedures. A modular adaptive geometry numerical model capable of simulating the propagation of laser light in a wide variety of multiple component tissues has been developed and tested. A material grid array is generated by assigning a value representing a tissue type to each of a large number of small voxels. The grid array is used to indicate optical properties in an existing variable step size, weighted-photon Monte Carlo algorithm that has been modified to account for voxels-to-voxels changes in optical properties. To test the model, simple geometric shapes and optical low coherence reflectometry images of rat skin have been used to create material grids consisting of epidermis, dermis, and blood. The model assumes 1-J/cm^2 irradiation of the tissue samples with a 1.0-mm diameter uniform beam at 585 nm. Computed results show good quantitative and qualitative agreement with published data. Various effects due to shading and scattering, similar to those suggested in the literature, are noted. This model provides a way to achieve more realistic representation of anatomical geometry as compared to other models, and produces accurate results.**

I. Introduction

NUMERICAL modeling of laser tissue interaction can be effective tools for understanding and improving laser treatments. Models enable the reseacher to visualize basic physical mechanisms—such as light absorption, temperature rise, and thermal damage—and to make computational "experiments" by varying laser parameters, tissue geometry, and thermal boundary conditions.

Modeling approaches to the general problems of light transport and heat transfer have been researched extensively. Techniques such as the Monte Carlo method [1] for optical modeling and finite difference or finite element methods [2] for thermal diffusion have been shown to be quite effective. However, the accuracy of laser tissue interaction numerical models is often called into question because they do not take into account the contribution of factors such as complex tissue geometry, water loss, thermal and mechanical damage, and dynamic changes in optical and thermal properties.

The distribution of light in turbid media was first described using the radiative transport equation [3] which cannot be solved analytically for most tissue geometries. Researchers have used techniques such as the diffusion approximation [4]–[6] and Beer's law [7], which are valid for highly scattering and nonscattering materials.

The Monte Carlo technique, an excellent overview of which is presented by Jacques and Wang [1], is a statistical method for simulating light transport that is valid for a wider variety of situations. Using experimentally determined absorption and scattering coefficients, Henyey–Greenstein anisotropy factors, indexes of refraction, and several physical and probabilistic relations, the photon "random walk" can be simulated repeatedly until a sufficient quantity of photons has been absorbed to establish reliable trends of energy deposition.

Previous research has shown that the Monte Carlo method can be used in different ways to effectively simulate laser irradiation of skin using homogeneous [8] and layered geometries [9]–[11]. Several studies have used the Monte Carlo technique to simulate treatment of port wine stain (PWS), combining simple geometric shapes to approximate the components of skin [8], [12]–[14]. Lucassen *et al.* [14] used layers, long cylinders, and long "curved vessels" to simulate the microstructure of skin. They reproduced some of the optical phenomena seen in laser-tissue interaction, including shading caused by more superficialvessels and how diffuse light fills partially shaded regions. Using layers and various sizes of straight, cylindrical vessels in a Monte Carlo model, Smithies *et al.* [13] demonstrated that changes in diameter and spatial distribution of blood vessels can affect energy deposition in skin more than a change in wavelength from 577 to 585 nm.

A two-dimensional (2-D) optical–thermal laser tissue interaction model has been developed by Kim [15] and Rastegar *et al.* [16]. The model iterates between Monte Carlo optical component and a finite-element thermal component to account for local changes in absorption and scattering coefficients due to temperature rise and thermal damage.

We have developed a three-dimensional (3-D) modular adaptive grid numerical model (MAGNUM) for light prop-

Manuscript received October 2, 1996; revised November 26, 1996. This work was supported in part by the Office of Naval Research Medical Free Electron Laser Biomedical Science Program under Grant N000 014-91-J1564, the Department of Energy Center of Excellence for Medical Laser Applications under Grant DE-FG03-95ER 61971, and the Albert W. and Clemmie A. Caster Foundation.

T. J. Pfefer, J. Kehlet Barton, E. K. Chan, M. G. Ducros, B. S. Sorg, and A. J. Welch are with the Biomedical Engineering Program, The University of Texas at Austin, Austin, TX 78712 USA.

T. E. Milner and J. S. Nelson are with the Beckman Laser Institute and Medical Institute, University of California at Irvine, Irvine, CA 92612-1475 USA.

Publisher Item Identifier S 1077-260X(96)09642-6.

agation in geometrically complex biological tissue. Although a modular representation of nonhomogeneous tissue would be useful in the simulation of any number of laser procedures, one obvious application is PWS treatment. Both clinical [17] and numerical studies [8], [13], [14] have shown that the specific vessel geometry plays a major role in determining the outcome of PWS treatment. Recent research has indicated that appropriate laser parameters depend on the unique 3-D mapping of PWS microstructure [18], [19].

This study has two goals: to digitally represent structurally complex biological tissue in a way that can be easily adapted to different geometries and to augment the standard Monte Carlo algorithm to handle three-dimensional (3-D), heterogeneous geometry.

II. Methods

A complete, yet concise description of algorithms added to a standard Monte Carlo model are covered in detail, while the basic Monte Carlo techniques are summarized.

A. Material Grid Generation

The key to the augmentation is a material grid which corresponds in size one-to-one with the grid that accumulates absorbed photon weights. In this grid, locations can be specified using Cartesian coordinates (x, y, z) or the indexes of a rectangular voxel (i, j, k). If all voxels are specified as cubes, a simple routine can be used to convert from Cartesian location to voxel index. The dimensions of the voxels ($\Delta x, \Delta y$, and Δz) and the number of elements in each direction ($i_{\max}$, $j_{\max}$, and $k_{\max}$) are used to establish the grid skeleton. The material grid is represented by an array in which each voxel is assigned an integer value corresponding to a material (in the case of skin: epidermis, dermis, or blood vessel).

Material grids were specified using two different techniques. The first set of grids was taken directly from geometry specified in the literature. These included a layered geometry (simulation 1) and a combination of layers and straight cylinders (simulations 2–5). The second set (simulations 6 and 7) was based on an *in vivo* blood vessel pair described by Barton *et al.* [20]. Subsurface high-resolution images of rat skin were acquired using optical low-coherence reflectometry (OLCR). The blood vessel outlines were manually traced from the images, and an epidermal layer of constant thickness was estimated. During the image-to-material grid conversion, irregularities in the curvature of the vessels were smoothed. In simulation 7, the vessels pair was duplicated, rotated approximately 90°, and placed below the original pair to illustrate asymmetric shading effects.

B. Photon Movement

An example of photon movement in two dimensions (x and z axes) is presented in Fig. 1. In the following description, references to Fig. 1 are enclosed in brackets.

The algorithm begins with the standard weighted photon "launch," which accounts for the beam profile and specular reflection. Initial directional cosines (μ_x, μ_y, and μ_z) are specified to represent light normal to the surface of the tissue.

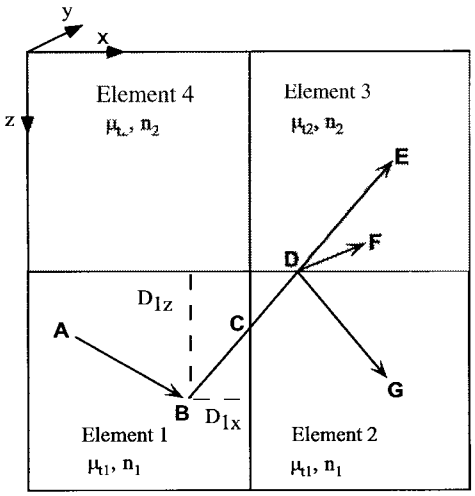

Fig. 1. Photon interaction with voxel boundaries in two dimensions. Segment AB shows photon movement when the entire path is contained within a single voxel. Segment BE shows the initial estimation of a photon path using optical properties of voxel 1, whereas BDF and BDG show the two final paths that are possible when material properties are considered: BDF when refraction and change in attenuation coefficient are accounted for and BDG when the photon is reflected. Points C and D indicate the location at which the photon crosses voxel boundaries.

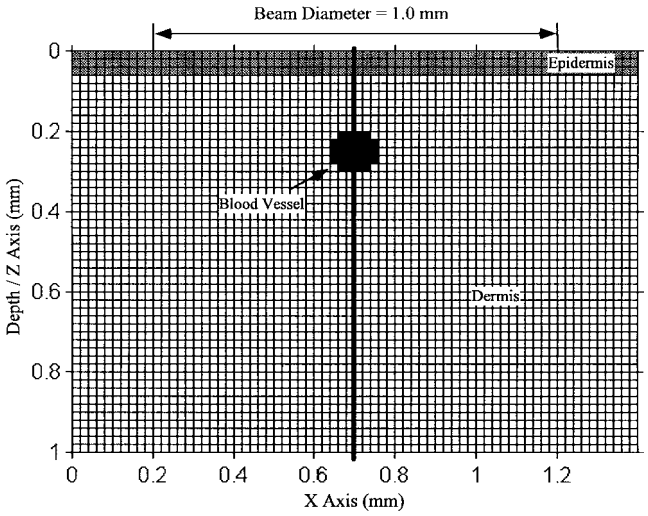

Fig. 2. Representation of xz plane cross section of material grid for simulation 2: 60-μm top epidermal layer and 940-μm dermal layer with single vessel with diameter of 120 μm. Voxel sides are 20 μm. The thick line denotes the edge of the graph in Fig. 3 and location of the data for the graph in Fig. 4.

Path lengths (S) are calculated using the local absorption (μ_a in cm^{-1}) and scattering coefficients (μ_s in cm^{-1}) and a random number. Using the present location (x, y, z) and directional cosines (μ_x, μ_y, and μ_z), the location within homogeneous tissue of the next potential attenuation event (x_p, y_p, z_p) is found

$$x_p = x + \mu_x * S$$
$$y_p = y + \mu_y * S$$
$$z_p = z + \mu_z * S.$$

The most significant augmentation of the Monte Carlo routine involved the movement of photons through elements and across their boundaries. Essentially, this required extending

the algorithm used for layered tissue into three dimensions. Movement within any voxel follows the standard algorithm for homogeneous tissue [segment AB]. When the size of the voxels is small with respect to penetration depth $(1/\mu_t$, where $\mu_t = \mu_a + \mu_s)$, it becomes unlikely that movement of distance S will be confined within a voxel.

In the case that the element of origin and potential end point voxel are different [as in segment BE], each point at which the photon exits, one voxel and enters another must be found. Based on the direction of the photon, three of the six planes defining a voxel can be eliminated as possible exit locations. The distances to each of the remaining planes (D_{nx}, D_{ny}, D_{nz}) and the directional cosines are used to calculate the partial path lengths (S_{nx}, S_{ny}, S_{nz}) that would have to be traveled to reach the planes. In the x direction, for example, if $\mu_x \neq 0$

$$D_{nx} = \left(x_{n,\text{center}} + \text{sign}(\mu_x)\frac{\Delta x}{2}\right) - x \quad S_{nx} = \frac{D_{nx}}{\mu_x}$$

if $\mu_x = 0$

$S_{nx} = \infty$ (photon will not exit voxel along x direction)

where $x_{n,\text{center}}$ is the center of voxel n and x is the original photon location. S_{ny} and S_{nz} are found by replacing x with y and z, respectively, in the above equations. [D_{1x} and D_{1z} are shown as dashed lines; S_{1x} corresponds to segment length BC; S_{1z} corresponds to segment length BD; if the photon is traveling only in the xz plane, $\mu_y = 0$ and $S_{1y} = \infty$]. The shortest of these partial path lengths [S_{1x}, segment length BC] defines the location of photon exit from the voxel (x', y', z'). If, for example, S_{nx} was the shortest

$$x' = x_{n,\text{center}} + \text{sign}(\mu_x)\frac{\Delta x}{2}$$
$$y' = y + S_{nx} * \mu_y$$
$$z' = z + S_{nx} * \mu_z.$$

The assignment of the location exactly on the voxel boundary (x' above) is made instead of using the equation $x' = x + S_{nx} * \mu_x$ in order to avoid problems due to potential rounding errors. The originally computed path length [BE] is then reduced by the distance traveled within element n [distance traveled in voxel 1, segment length BC]

$$S' = S - S_{nx}.$$

If the new path length (S') [segment CE] indicates that another voxel boundary must be crossed, the photon is propagated from one voxel boundary to the next [segment CD]; this sequence is repeated until the photon can be propagated from a voxel boundary to the location of the attenuation event [segment DE, assuming $\mu_{t1} = \mu_{t2}$ and $n_1 = n_2$] or reaches the boundary of the tissue.

Upon entering a voxel with a different attenuation coefficient μ_t', S is rescaled according to the ratio of the attenuation coefficients

$$S' = S * \frac{\mu_t}{\mu_t'}.$$

(The effect of rescaling is seen in the difference in length between segments DF and DG, assuming $\mu_{t1} < \mu_{t2}$). The initially computed optical distance (in dimensionless units of optical depth) is equal to the sum of the optical distances traveled in each of the n voxels

$$(\mu_t * S)_{\text{initial}} = \sum_n (\mu_{tn} * S_n).$$

Changes in the index of refraction are accounted for differently at tissue–tissue and air–tissue interfaces. If a photon encounters an index of refraction change between tissue types (interface between voxels 2 and 3 at point D) and the angle of the photon with the incident surface is larger than the critical angle, the photon is reflected. At angles less than the critical, the Fresnel equation and a randomly generated number are used to determine if the photon is reflected (segment DG) or transmitted through the interface and is refracted (segment DF). If the surface is parallel to the xy plane, for example, refraction alters the directional cosines as follows:

$$\mu_x' = \mu_x \frac{n_i}{n_t} \quad \mu_y' = \mu_y \frac{n_i}{n_t} \quad \mu_z' = \text{sign}(\mu_z)\cos\Theta_t$$

where Θ_t is calculated from Snell's Law: $(n_i \sin\Theta_i = n_t \sin\Theta_t)$, and subscripts i and t indicate the incident and transmitted sides of the interface. At the air–tissue interface, the critical angle determines total internal reflection, whereas the Fresnel equation is used to determine the fraction of the photon weight that escapes. The remaining weight is reflected back into the tissue.

If a photon travels the entire path length without escaping, the standard Monte Carlo absorption, Henyey–Greenstein scattering, and roulette termination procedures are used. Each absorption is recorded and used to calculate the local energy deposition (J/cm^3).

TABLE I
TISSUE OPTICAL PROPERTIES FOR 585 NM, FROM LUCASSEN *ET AL.* [14]

Tissue Type	μ_a (cm^{-1})	μ_s (cm^{-1})	g (cm^{-1})	n (cm^{-1})
Epidermis	18	470	0.790	1.37
Dermis	2.2	129	0.790	1.37
Blood Vessel	191	468	0.995	1.33

C. Simulations of Skin with Blood Vessels

In all of the vessel simulations (2–7), several basic parameters remain the same. Cubic voxels are used. The size of the tissue samples being modeled is 1.4 mm × 1.4 mm × 1.0 mm. The top 60 μm represents a layer of epidermis, with the remaining 940 μm are comprised of dermis and the specified blood vessels. The laser wavelength of 585 nm, a flat top profile, a fluence of 1 J/cm^2, and a diameter of 1.0 mm are assumed. The beam is centered at $x = 700$ μm, $y = 700$ μm, $z = 0$ μm. Optical properties used in this model are displayed in Table I. The index of refraction of air ($n = 1.0$) was used at the boundaries. Simulations were performed using 10 000 000 photons.

III. RESULTS

The seven simulations detailed in this section have been divided into two parts. Simulations 1–5 use highly simplified geometries (one with layers only, four with straight vessels)

TABLE II
COMBINATIONS OF PARAMETERS USED IN VESSEL SIMULATIONS

Simulation	Number of Voxels	Number of Vessels	Depth of Vessel Center(s) (μm)	Vessel Geometry
2	70 x 70 x 50	1	250	Straight
3	140 x 140 x 100	1	250	Straight
4	140 x 140 x 100	1	500	Straight
5	140 x 140 x 100	2	250, 500	Straight
6	140 x 140 x 100	2	365	OCT-based
7	140 x 140 x 100	4	365, 615	OCT-based

TABLE III
DIFFUSE REFLECTANCE AND TRANSMISSION FOR SIMULATION 1. *FROM CHAN *ET AL.* [21] ** MAGNUM RESULTS FROM FIVE RUNS OF 10 000 PHOTONS (AVERAGE +/− STANDARD DEVIATION)

Source (# of Photons)	Diffuse Reflectance (%)	Transmission (%)
Measurements*	21.06	50.00
L. Wang Model* (10,000)	21.26	49.54
MAGNUM ** (50,000)	21.25 +/- 0.19	49.88 +/- 0.17

similar to that found in the literature. Simulations 6 and 7 employ more complex, anatomically realistic OLCR image-derived geometry. An overview of the parameters used in the six simulations using vessel geometry (simulations 2–7) is given in Table II.

A. Simplified Geometry Simulations

Simulation 1 involves a semi-infinite (in xy plane) three-layer slab configuration specified by Chan *et al.* [21], consisting of 1.0 mm of glass (nonabsorbing, nonscattering, $n = 1.54$), 700 μm of skin ($\mu_s = 14.16$ cm^{-1}, $\mu_a = 1.36$ cm^{-1}, $g = 0$, $n = 1.38$), and another 1.0 mm of glass, surrounded by air ($n = 1.0$). The fraction of diffuse reflectance and transmission of the laser light as predicted by MAGNUM in five trials of 10 000 photons is shown in Table III, along with corresponding data experimental and modeled from Chan *et al.* [21].

The geometries for simulations 2–5 use one or two straight, cylindrical blood vessels running parallel to the y axis, directly below the laser beam. The goal of these simulations is to assess MAGNUM's accuracy by analyzing the effect of a change in grid resolution and comparing MAGNUM's results with simulations from the literature. Since symmetric geometries are used in simulations 2–5, only half the tissue slice is shown in the surface plots.

The geometry for simulation 2 (Fig. 2) involves a 120-μm diameter vessel located at a depth of 250 μm. Since the size of the voxels (20 μm on a side) that specify the material grid are on the same order as the cylinder diameter, there is noticeable distortion from the desired circular shape. The distribution of energy deposition in the xz plane at $y = 700$ μm is shown in Fig. 3. The energy deposited in the column of cubes directly below the center of the beam ($x = y = 700$ μm) is illustrated in Fig. 4.

The material grid cross section shown in Fig. 5 shows the geometry for simulations 3–5. Epidermal and dermal layers and two vertically aligned cylindrical vessels of the same size as in simulation 2 (120-μm diameter) are represented using cubes measuring 10 μm on a side. Smaller voxel size results in higher resolution and improved representation of the circular nature of the vessel. Simulation 3 uses the superficial vessel only, simulation 4 uses the deeper vessel only, and simulation 5 uses both vessels as displayed.

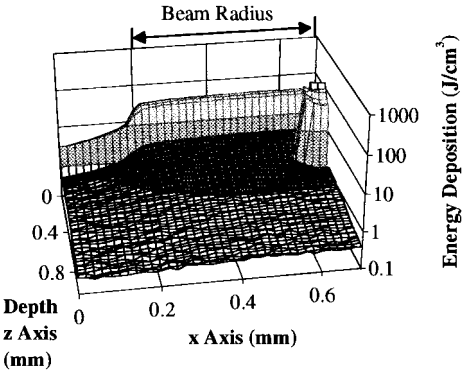

Fig. 3. Surface plot of energy deposition (J/cm^3) for the xz plane cross section at beam center ($y = 700$ μm) for the geometry of Fig. 2.

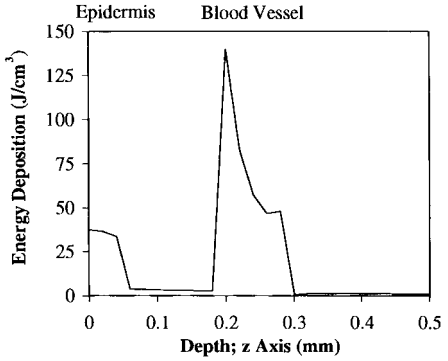

Fig. 4. Line graph of energy deposition versus depth at beam center from data in Fig. 3 (see vertical line in Fig. 2).

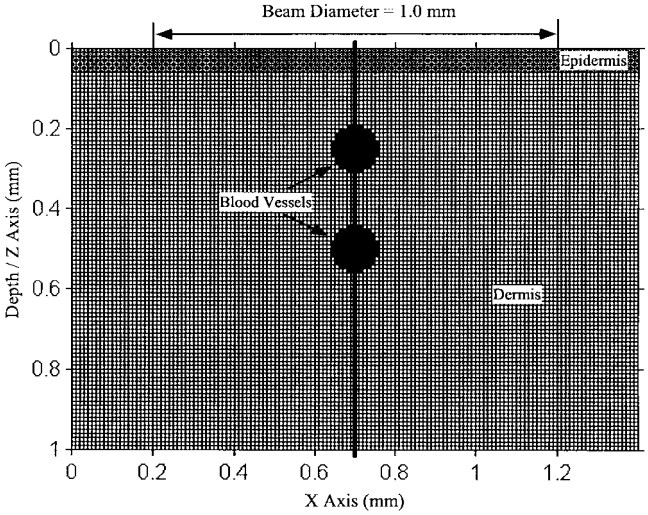

Fig. 5. Representation of xz plane cross section of material grid for simulations 3–5: 3 uses the superficial ($z_{\text{center}} = 250$ μm) vessel only, 4 uses the deep ($z_{\text{center}} = 500$ μm) vessel only, and 5 uses both vessels. All simulations include a 60-μm top epidermal layer, 940-μm dermal layer with vessels with diameter of 120-μm, and cubic voxels with 10-μm sides. The thick line denotes the edge of the graphs in Fig. 6 and the location of the data for graph the in Fig. 7.

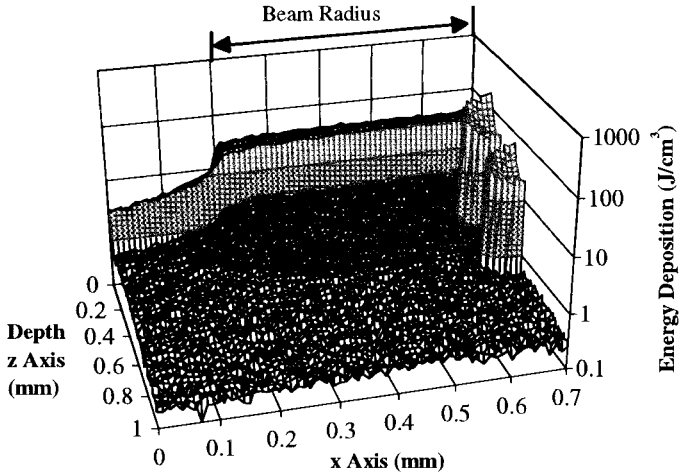

Fig. 6. Surface plot of energy deposition for the xz plane cross section at beam center ($y = 700$ μm) for simulation of two 120-μm diameter vessels depicted in Fig. 5.

Due to increased resolution, energy deposition results from simulation 5 (Fig. 6) show a more realistic distribution in the blood vessel than seen in simulation 2 (Fig. 3). The statistical variation in the dermis has increased due to a decrease in the photon deposition per voxel. The surface plot of simulation 5 results (Fig. 6) shows no effect of direct shading on the deeper vessel, but less energy is deposited than in the superficial vessel. Energy deposition results for simulations 3–5 are shown as a function of tissue depth below the beam center in Fig. 7. To minimize the statistical variation of the graphs in Fig. 7, for each data set the two columns of voxels on either side of the laser beam center (see thick line in Fig. 5) were averaged. Fig. 7(a) uses a linear scale to provide a direct comparison with data from the literature and to show the effect of shading on energy deposition in blood vessels. Fig. 7(b) uses a logarithmic scale to illustrate the effects of shading on the dermis and, indirectly, the scattering-induced recovery of the fluence.

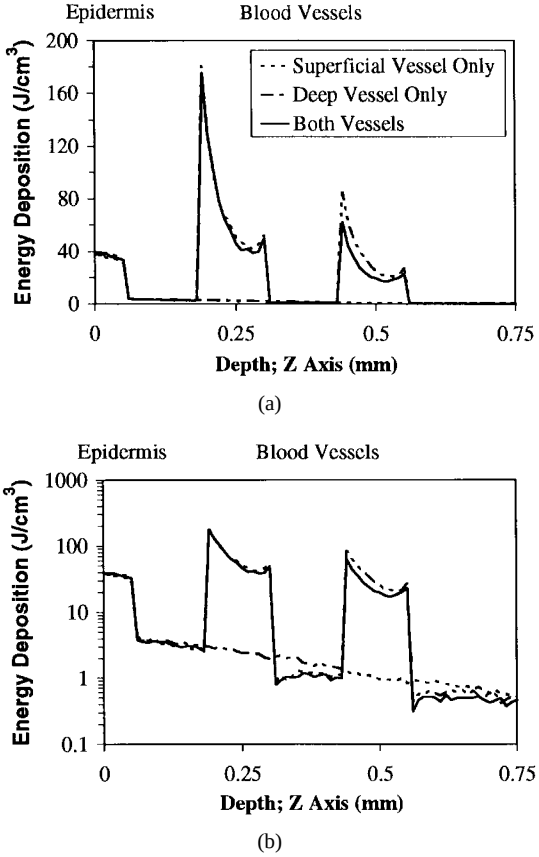

Fig. 7. Line graphs of energy deposition versus depth at beam center for simulations with a single, 120-μm diameter vessel at depth of 250 μm (dotted line), single vessel at depth of 500 μm (dashed line), and both vessels as illustrated in Fig. 5 (solid line). (a) Linear scale for comparison with data from literature and to illustrate effect of shading on vessels and epidermis. (b) Logarithmic scale to illustrate effect of shading on dermis and scattering-induced "recovery" below vessels.

B. Simulations Using OLCR Image-Based Geometry

The geometries for the final two simulations were adapted from OLCR images of blood vessels in rat skin. The material grid top view in Fig. 8(a) and cross section in Fig. 8(b) show the four vessels used in simulations 6 and 7. The two sets of roughly perpendicular vessel pairs were used in simulation 7, whereas only the superficial pair was used in simulation 6. Each vessel pair is comprised of a 90-μm diameter vessel and a 190-μm diameter vessel (the diameters of the superficial and deep vessels are specified in the xz and yz planes, respectively). The superficial and deeper vessel pairs are centered at depths of 365 μmand 615 μm, respectively.

The results for simulation 6 were very similar to that of the superficial vessel pair in simulation 7 and are, therefore, not presented. This data can be inferred from Figs. 9 and 10.

Simulation 7 used the most complex geometry, involving two layers of OLCR-specified vessel pairs at different depths, with the primary intent of investigating optical mechanisms with more realistic, complex vessel geometry. Fig. 9 shows a shading-induced decrease in energy deposition along the top surface of the larger deep vessel. The line graph of energy deposition at the depths of the vessel pair centers (365 μm and 615 μm) seen in Fig. 10 shows greater variation in the larger vessel than the smaller one for each vessel pairand asymmetric distributions of deposited energy in each of the deeper vessels.

IV. Discussion

There are three main issues to be addressed in evaluating MAGNUM: the effect of modularization of the material grid on the representation of vessel geometry and the results, the quality of the data insofar as the data compares to that found in the literature, and computational considerations.

A. Reproduction of Tissue Geometry

A main goal of this research is to maximize accuracy when developing representations of 3-D tissue geometries. Since MAGNUM relies on cubic voxels to build tissue structures, it cannot specify rounded edges as well as can be done using geometric shapes such as cylinders. To adequately represent the curvature of a region, voxel size must be much smaller than the region or the true geometry will be lost. Reducing the voxel size brought about a significantly better representation of

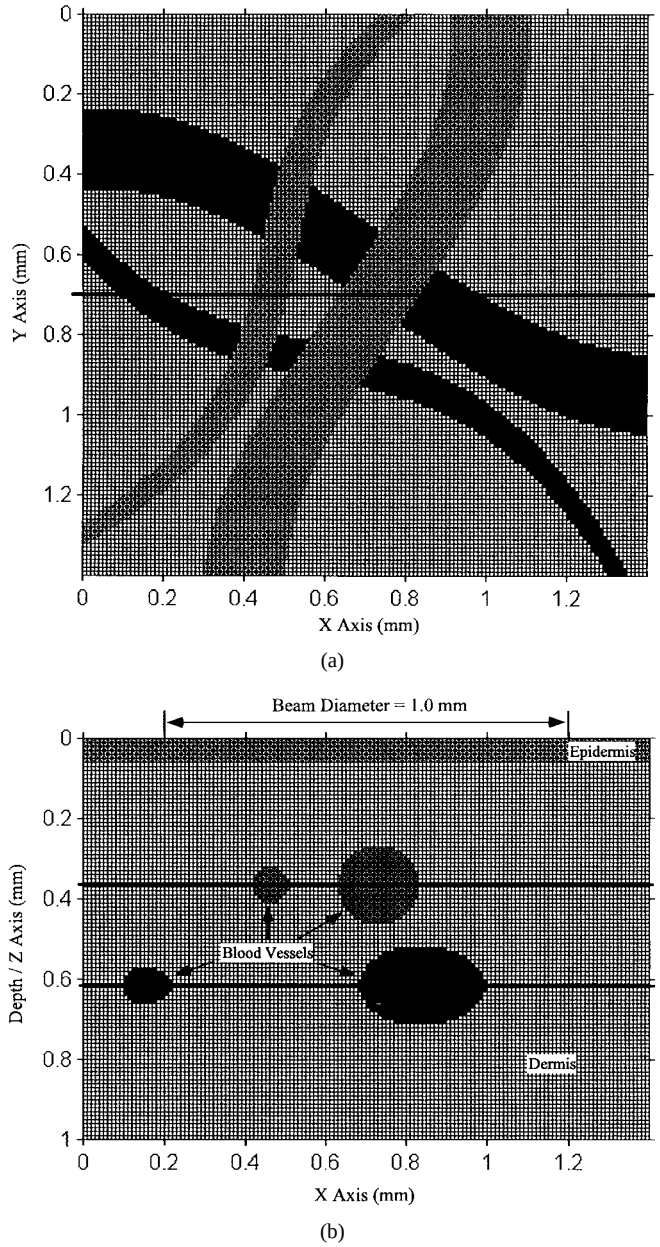

Fig. 8. (a) Top view (xy plane) of material grid representation ($\Delta x = \Delta y = \Delta z = 10$ μm) with four blood vessels derived from an OLCR image of rat skin. Simulation 6 was performed using only the superficial vessel pair, whereas simulation 7 used both pairs. The thick line denotes location of cross section for Figs. 8(b) and 9. (b) Representation of xz plane cross section of material grid at beam center ($y = 700$ μm). Thick lines denote location of data sets for Fig. 10 (at depth of vessel centers, $z = 365$, 615 μm).

the curvature of the vessel. Higher resolution also led to a more accurate, continuous distribution of absorbed energy within the vessel, although statistical variation increased (most noticeably in the dermis) due to a factor of eight decrease in the average number of photons absorbed in each voxel. In choosing a voxel yvsize, both the resolution needed to properly represent structures and the statistical variation due to small voxel size must be considered in order to find an appropriate balance. If computation time and memory size limits the minimum voxel size to 10 μm, then the cross section of a 10-μm vessel would be represented by a single voxel. Note that the smallest vessels are 10 μm or larger. Choice of grid parameters is a basic issue of modeling which will be discussed further in the section on computational considerations.

B. Comparison with Modeled Results from the Literature

Simulations 1–5 give good evidence of MAGNUM's ability to simulate the basic optical mechanisms of absorption, scattering, reflection, and refraction. The transmission and diffuse reflection results produced by MAGNUM for the simplified case in simulation 1 were within 1% of data calculated using a well-established Monte Carlo model by Wang and Jacques [9] and within 2% of experimental values found by Chan *et al.* [21].

The results from simulations 2–5 can be compared to studies that used similar geometries with simple straight cylindrical vessels [13], [14], [22]. Due to differences in methodology, laser parameters, and inability to read specific data points from contour plots, it is difficult to make direct comparisons in most cases. Therefore, trends in energy deposition in the epidermis, dermis, and blood vessels will be compared.

Results from MAGNUM and those from two other studies [13], [14] exhibit numerous common features that can be attributed to absorption, scattering, and/or shading effects. One example is the energy deposition in the epidermis, which decreases steadily by a few percent over its 60-μm thickness, with its magnitude comparable to the peak in deeper vessels in simulations 4 and 5, whereas in superficial vessels from simulations 2, 3, and 5, the peak is about 3 to 4 times greater than the level in the epidermis. Additionally, the epidermal layer tends to be affected only minimally by adding vessels in the dermis.

In these models, distribution of energy absorbed in the vessels is seen to be affected by several mechanisms. The primary influence is the large μ_a of blood at 585 nm, which is an order of magnitude greater than the μ_a of epidermis. Because of the short penetration depth ($1/\mu_t = 15$ μm) in blood at 585 nm, a large quantity of energy is absorbed at the outer, top edge of the vessels and a radial gradient (sharp, exponential decrease toward the center) in absorbed energy is seen. The light directionality also plays an important role. If a vessel is directly below the beam center, the gradients are strongest in the z direction (depth), whereas for a vessel located to one side of the beam, the gradients are directed at an angle (see Figs. 9 and 10). Smaller vessels exhibit a more constant distribution of absorbed energy over their cross section (see Fig. 10) because the number of photons that reache the middle of the vessel is proportional to the distance they must travel through highly absorbing blood.

Scattering also leads to features observed in all of the simulations. Because of scattering, collimated laser light becomes diffuse. Thus, photons also impact a vessel from the bottom and sides, causing a peak along the peripheral walls of the vessels. Below a highly absorbing vessel, scattering in the dermis quickly diminishes the effect of direct shading [Fig. 7(b)]. Although this leads to a distributed decrease in the magnitude of energy deposition in the tissue, gradients remain unaffected except in a small region directly behind the vessel.

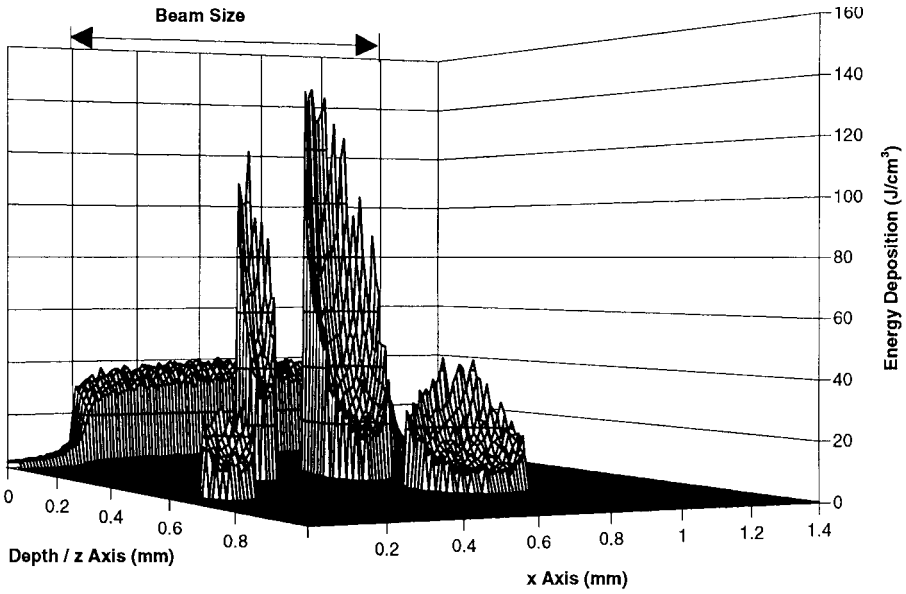

Fig. 9. Surface plot of energy deposition for the xz plane cross section at beam center ($y = 700$ μm) for four vessel geometry in Fig. 8. Superficial vessels had diameters of 90 and 190 μm. Deeper vessels, although circular in yz plane cross section, are seen as elliptical in xz plane cross section.

The only instance of vessel shading is seen in Figs. 9 and 10, in which the larger of the deeper vessels shows a significant decrease in energy deposition over a region directly below the larger superficial vessel.

Probably the most interesting comparison can be made with Fig. 7(a) from this paper and Fig. 4(b) from Lucassen *et al.* [14]. The graphs show agreement within a few percent for the distribution of energy deposition in the epidermis for all three cases and in the vessels for the single superficial and single deep vessel cases. However, according to MAGNUM the energy deposition in the superficial blood vessel for the two vessel case is only slightly reduced from the single vessel case. Data published by Lucassen *et al.* [14] indicates that the addition of a deeper vessel significantly affects energy deposition in the more superficial vessel. Therefore, in all but one instance MAGNUM's data is in good quantitative and qualitative agreement with the literature.

C. Computational Effectiveness

MAGNUM was developed as a step toward a complex type of laser tissue interaction model—one which requires a great deal of computational power. In order to represent a sizable volume of tissue in three dimensions with high resolution and record the distribution of absorbed photons, it is necessary to use large material and energy deposition arrays. In the most extensive simulations performed (3–7), this involved matrices with dimensions of $140 \times 140 \times 100$, for a total of nearly 2 million elements per array. The propagation of 10 000 000 photons required approximately 1000–1500 minutes of processor time on an IBM RS/6000 workstation.

When considering MAGNUM's computational effectiveness, the relationship between data resolution and noise level, inputs such as grid and voxel size, number of photons, and computational considerations such as memory and processor time, must be considered. Increasing the resolution of a model imposes greater demands on memory size. In the change from simulation 2 to 3, the number of elements in the material and absorption matrices went from 245 000 to 1 960 000, each. With increased resolution came increased statistical variation since there were fewer photons deposited per bin. In order to increase resolution and maintain accuracy, a proportional increase in the number of photons is needed, and, consequently, more processor time. Therefore, when setting input parameters relating to grid size and number of photons, it is worthwhile to consider the goal of the simulation and the limitations of the computer system.

This study has presented energy deposition data for various tissue geometries. A thorough analysis of PWS laser treatment will require the addition of a finite difference or finite element method component for computation of heat conduction. The energy deposition (J/cm^3) from the Monte Carlo model is used as the source term in thermal models that compute the transient temperature response. Such a model should have the capability of accounting for nonhomogeneous tissue, various types of boundary conditions, the cooling effect of perfusion, and changes in perfusion due to thermal damage [23], as well as dynamic changes in optical and thermal properties. Thermal damage can be predicted by including a temperature, time-dependent rate process [24].

It should be noted that accurate communication of four (or more) dimensions of data in a 2-D black and white (or color) format is difficult, if not impossible. The ability to view and graphically manipulate complex, multidimensional data sets would greatly enhance one's comprehension of the information. Until such a format is available to facilitate mass communication of data among researchers, the scientific community as a whole will remain at a significant disadvantage.

V. Conclusion

This augmented Monte Carlo technique will allow better representation of real biological tissues and lead to improved

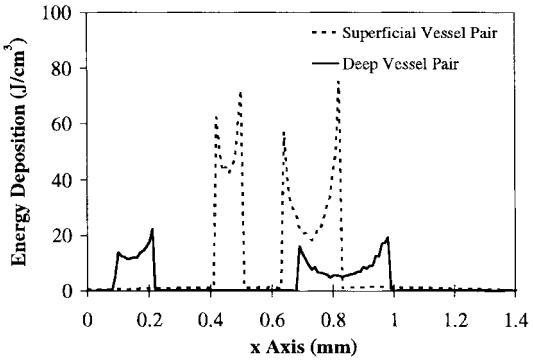

Fig. 10. Line graph of energy deposition through upper and lower vessel centers over x axis at constant depth of 365 and 615 μm [see Fig. 8(b)], for data in Fig. 9.

simulation of laser surgery procedures. Although the concept of modularization is not new, this is the first time, to the authors' knowledge, that it has been applied to optical modeling of complex, 3-D, anatomical structures. Good approximation of skin tissue with PWS can be accomplished, although care must be taken to use the proper resolution when specifying small, curved vessels. Benchmarking against data from the literature has helped to establish that MAGNUM can provide qualitatively and quantitatively reliable energy deposition information.

The cost of this improvement of the Monte Carlo technique is an increase in computational requirements. Access to a workstation of moderate speed and memory size is highly recommended when using MAGNUM with a moderate- to high-resolution grid. Future improvements in the model will most likely necessitate even greater computational power.

In order to raise MAGNUM to a level at which meaningful simulation is possible, two advancements are planned. First, real tissue geometries will be reconstructed by converting digitized pictures of histology or confocal and coherence-domain system images into material grids on a pixel-by-pixel basis. Second, a thermal component that incorporates the capabilities mentioned in Section IV will be added to MAGNUM.

ACKNOWLEDGMENT

The authors wish to thank E. Duco Jansen and A. Dunn for their support in editing this paper.

REFERENCES

[1] S. L. Jacques and L. Wang, "Monte Carlo modeling of light transport in tissues," in *Optical-Thermal Response of Laser-Irradiated Tissue*, A. J. Welch and M. J. C. vanGemert, Eds. New York: Plenum, 1995.
[2] J. Roider and R. Birngruber, "Solution of the heat conduction equation," in *Optical-Thermal Response of Laser-Irradiated Tissue*, A. J. Welch and M. J. C. vanGemert, Eds. New York: Plenum, 1995.
[3] S. Chandrasekhar, *Radiative Transfer*. New York: Dover, 1960.
[4] A. Ishimaru, *Wave Propagation and Scattering in Random Media*, vol. 1. New York: Academic, 1978.
[5] B. Kim, S. L. Jacques, S. Rastegar, S. Thomsen, and M. Motamedi, "The role of dynamic changes in blood perfusion and optical properties in thermal coagulation of the prostate," in *Proc. SPIE*, 1995, vol. 2391, pp. 443–450.
[6] B. Anvari, S. Rastegar, and M. Motamedi, "Modeling of intraluminal heating of biological tissue: Implications for treatment of benign prostatic hyperplasia," *IEEE Trans. Biomed. Eng.*, vol. 41, no. 9, pp. 854–864, 1994.
[7] A. Sagi, A. Shitzer, A. Katzir, and S. Akselrod, "Heating of biological tissue by laser irradiation: Theoretical model," *Optical Engineering*, vol. 31, no. 7, pp. 1417–1424, 1992.
[8] M. Keijzer, S. L. Jacques, S. A. Prahl, and A. J. Welch, "Light distributions in artery tissue: Monte Carlo simulations for finite-diameter laser beams," *Lasers Surg. Med.*, vol. 9, pp. 148–154, 1989.
[9] L. Wang and S. L. Jacques, "Monte Carlo modeling of light transport in multi-layered tissues in standard C," Univ. Texas, M. D. Anderson Cancer Center, 1992.
[10] I. D. Miller and A. R. Veitch, "Optical modeling of light distributions in skin tissue following laser irradiation," *Lasers Surg. Med.*, vol. 13, pp. 565–571, 1993.
[11] B. Nemati, "Transcleral argon cyclophotocoagulation: A preclinical study," Ph.D. dissertation, Univ. Texas at Austin, 1995.
[12] M. J. C. vanGemert, A. J. Welch, J. W. Pickering, O. T. Tan, and G. H. M. Gijsbers, "Wavelengths for laser treatment of port wine stains and telangiectasia," *Lasers Surg. Med.*, vol. 16, pp. 147–155, 1995.
[13] D. J. Smithies and P. H. Butler, "Modeling the distribution of laser light in port-wine stains with the Monte Carlo method," *Phys. Med. Biol.*, vol. 40, pp. 701–731, 1995.
[14] G. W. Lucassen, W. Verkruysse, M. Keijzer, and M. J. C. vanGemert, "Light distributions in a port wine stain model containing multiple cylindrical and curved blood vessels," *Lasers Surg. Med.*, vol. 18, pp. 345–357, 1996.
[15] B. Kim, "An analysis of the effects of coupling between temperature rise and light distribution in laser irradiated tissue using finite element and Monte Carlo methods," Masters thesis, Texas A&M Univ., 1991.
[16] S. Rastegar, B. Kim, and S. L. Jacques, "Role of temperature dependence of optical properties in laser irradiation of biological tissue," in *Proc. SPIE*, 1992, vol. 1646, pp. 228–231.
[17] J. M. Noe, S. H. Barsky, D. E. Geer, and S. Rosen, "Port wine stains and the response to argon laser therapy: Successful treatment and the predictive role of color, age, biopsy," *Plastic Reconstructive Surg.*, vol. 65, no. 2, pp. 130–136, 1980.
[18] M. J. C. vanGemert, J. S. Nelson, T. E. Milner, D. J. Smithies, W. Verkruysse, J. F. de Boer, G. W. Lucassen, D. M. Goodman, B. S. Tanenbaum, L. T. Norvang, and L. O. Svaasand, "Non-invasive determination of port wine stain anatomy and physiology for optimal laser treatment strategies," *Phys. Med. Biol.*, in press.
[19] M. J. C. vanGemert, D. J. Smithies, W. Verkruysse, T. E. Milner, and J. S. Nelson, "Wavelengths for port wine stain laser treatment: Influence of vessel radius and skin anatomy," *Phys. Med. Biol.*, in press.
[20] J. K. Barton, T. E. Milner, T. J. Pfefer, J. S. Nelson, and A. J. Welch, "Feasibility of using optical low coherence reflectometry to enhance optical modeling of skin," *J. Biomedical Optics*, to be published.
[21] E. Chan, B. Sorg, D. Protsenko, M. O'Neil, M. Motamedi, and A. J. Welch, "Effects of compression on soft tissue optical properties," this issue, pp. 943–950.
[22] M. Keijzer, J. W. Pickering, and M. J. C. vanGemert, "Laser beam diameter for port wine stain treatment," *Lasers Surg. Med.*, vol. 11, pp. 601–605, 1991.
[23] I. A. Lubashevsky, A. V. Priezzhev, V. V. Gafiychuk, and M. G. Cadjan, "Free boundary model for local thermal coagulation," in *Proc. SPIE*, 1996, vol. 2681, pp. 81–91.
[24] J. Pearce and S. Thomsen, "Rate process analysis of thermal damage," in *Optical-Thermal Response of Laser-Irradiated Tissue*, A. J. Welch and M. J. C. vanGemert, Eds. New York: Plenum, 1995.

T. Joshua Pfefer received the B.S. degree in mechanical engineering from Northwestern University, Evanston, IL, in 1991, and the M.S. degree in mechanical engineering from the University of Texas at Austin, in 1993.

Since 1994, he has held Research Assistant and Teaching Assistant positions while pursuing the Ph.D. in the Biomedical Engineering Program at the University of Texas at Austin. His research interests include optical and thermal numerical modeling of laser tissue interaction, thermal mechanisms of pulsed laser ablation, and transmyocardial laser revascularization.

Jennifer Kehlet Barton (S'95) received the B.S. degree from the University of Texas at Austin, and the M.S. degree from the University of California, Irvine, both in electrical engineering.

She worked for five years at McDonnell Douglas, Huntington Beach, CA, designing lighting systems for the International Space Station. She is currently an A. D. Hutchinson and NASA/Texas Space Grant Consortium Fellow at the University of Texas at Austin studying toward the Ph.D. degree in Biomedical Engineering. She is a member of Tau Beta Pi.

Eric K. Chan received the B.S. and M.S. degrees from the University of Rochester, both in optics. He is currently a Ph.D. candidate at The University of Texas (UT) at Austin.

Before he joined UT, he was a laser processing engineer with Bausch & Lomb Corporation, Rochester, NY, where he helped automate an excimer laser system for profiling contact lenses. His research interests include laser material processing, tissue optics and minimally invasive optical techniques for diagnostics and therapeutics.

Mr. Chan is a member of SPIE, the Optical Society of America, Tau Beta Pi, and Phi Kappa Phi.

Mathieu G. Ducros received the Engineering Diploma from Ecole Centrale de Lille, France, in 1995, the M.S. degree in biomedical engineering from the University of Texas at Austin in 1996, and is currently pursuing the Ph.D. degree in the Biomedical Engineering Program, University of Texas at Austin.

His interests are optical imaging and laser-tissue interactions. His research area is mainly optical coherence tomography.

Brian S. Sorg received the B.S. degree in electrical engineering at the University of Maryland, College Park, in 1992, the M.S. degree in biomedical engineering from the Johns Hopkins University, Baltimore, MD, in 1995, and is currently pursuing the Ph.D. degree in biomedical engineering at the Unversity of Texas at Austin.

His research interests include diagnostic and therapeutic applications of optics and lasers. Mr. Sorg is a member of Tau Beta Pi.

Thomas E. Milner, photograph and biography not available at the time of publication.

J. Stuart Nelson, photograph and biography not available at the time of publication.

Ashley J. Welch (M'66–SM'79–F'91) received the B.E.E. degree from Texas Tech University in 1955 and the M.S. degree in electrical engineering from SMU in 1959. He received the doctorate degree from Rice University in 1964.

He joined the University of Texas as an Assistant Professor in 1964. Currently, he is a Professor of electrical and computer engineering and is the Marion E. Forsman Centennial Professor of Electrical and Computer Engineering and Biomedical Engineering at the University of Texas at Austin.